Journal Pre-proof

Exploring the mechanism of stress-induced passive layer degradation in additively manufactured Ni-Fe-Cr-based alloy 718

Arshad Yazdanpanah, Reynier I. Revilla, Mattia Franceschi, Gioele Pagot, Mona Khodabakhshi, Iris De Graeve, Vito Di Noto, Manuele Dabalà, Sergio Lozano-Perez

Please cite this article as: Arshad Yazdanpanah, Reynier I. Revilla, Mattia Franceschi, Gioele Pagot, Mona Khodabakhshi, Iris De Graeve, Vito Di Noto, Manuele Dabalà and Sergio Lozano-Perez, Exploring the mechanism of stress-induced passive layer degradation in additively manufactured Ni-Fe-Cr-based alloy 718, *Corrosion Science,* (2024)
doi:https://doi.org/10.1016/j.corsci.2024.112523

This is a PDF file of an article that has undergone enhancements after acceptance, such as the addition of a cover page and metadata, and formatting for readability, but it is not yet the definitive version of record. This version will undergo additional copyediting, typesetting and review before it is published in its final form, but we are providing this version to give early visibility of the article. Please note that, during the production process, errors may be discovered which could affect the content, and all legal disclaimers that apply to the journal pertain.

Exploring the mechanism of stress-induced passive layer degradation in additively manufactured Ni-Fe-Cr-based alloy 718

Arshad Yazdanpanah[a]*, Reynier I. Revilla[b]*, Mattia Franceschi, Gioele Pagot[a], Mona Khodabakhshi[a], Iris De Graeve[b], Vito Di Noto[a], Manuele Dabalà[a], Sergio Lozano-Perez[d]

[a] Department of Industrial Engineering, University of Padova, Via Marzolo 9, 35131 Padova, Italy

[b] Vrije Universiteit Brussel, Department of Materials and Chemistry (MACH), Research Group Sustainable Materials engineering (SUME)

c Department of Engineering and Management, University of Padova, Stradella San Nicola 3, 36100 Vicenza, Italy

[d] Department of Materials, University of Oxford, Parks Road, OX1 3PH Oxford, UK

Corresponding authors: arshad.yazdanpanah@phd.unipd.it

rrevilla@vub.be

Abstract

This study explores the formation and degradation mechanisms of the passive layer on laser powder bed fusion (L-PBF) processed Ni-Fe-Cr-based alloy 718 using high-resolution submicron analysis and microcapillary electrochemical techniques. The findings provide new insights into passive layer breakdown under tensile loading, revealing the influence of microstructural characteristics, dislocation distribution, and mechanical stresses. Tensile loading caused oxide layer cracking near cell boundaries with higher dislocation density. Detachment of the oxide layer from the matrix created voids, allowing aggressive ions to penetrate, promoting crevice corrosion. Cell boundaries remained mostly intact, as metallic particles within the surface oxide layer.

Keywords:

Metal additive manufacturing; Ni-Cr-based alloy; Corrosion; Passivity; Stress corrosion; Microstructural analysis

1. Introduction

Over the past decade, metal additive manufacturing (MAM) has attracted considerable attention for its ability to produce complex geometries at reduced cost and time compared to traditional methods [1–3]. This has prompted exploration of its potential across industries such as chemical, petrochemical, gas and oil, and nuclear, for component production of substitution part or development of new geometries [4]. Laser powder bed fusion (L-PBF) has emerged as one of the most advanced additive manufacturing techniques, capable of producing parts with almost full density. In certain cases, the metastable microstructures consist of submicron cellular or columnar structures, with decorated cell boundaries influenced by alloying elements [5–9]. Ni-Cr-based super alloys are mainly used in critical industries due to their great performance in corrosion resistance, while alloy 718 is a variant of the Ni-Cr-based alloys which is widely used in petroleum, energy, and nuclear industries due to their great corrosion and mechanical performance.

A significant concern in critical industries is whether MAM parts exhibit comparable corrosion and stress corrosion cracking (SCC) resistance to conventionally produced materials. Despite extensive research, an agreement regarding the performance of MAM processed materials relative to their conventionally produced counterparts remains elusive for various material types, including austenitic stainless steels and nickel-based alloys. This lack of agreement is primarily attributed to the substantial variability in process parameters across different studies. For instance, in the case of alloy 718, Stachowiak et al. [10] reported significantly improved tribocorrosion performance of L-PBF 718 compared to conventionally manufactured material. This enhancement is attributed to a more compact passive layer, which results from the finer grain size and the absence of hard secondary particles in the additively manufactured material. Murmey et al. [11] reported improved corrosion performance of L-PBF 718 after solution annealing and aging treatments, resulting in a microstructure similar to conventional alloy 718. This enhancement was attributed to the higher grain size compared to the as-built state. On the other hand, Shi et al. [12] reported inferior corrosion resistance of L-PBF processed alloy 718 in molten salt, attributing this to intrinsic defects present at grain boundaries. Conversely, Mythreyi et al. [13] found that the as-built state exhibited superior corrosion resistance compared to its solution-annealed and double-aged counterpart. This was attributed to the presence of secondary phases in the double-aged material, which increased the risk of corrosion adjacent to these phases. Thuneman et al. [14] also reported better corrosion performance of L-PBF material compared to the double-aged conventional counterpart. This improvement was

attributed to the absence of secondary precipitates (γ' and γ'') in the as-built state, which was also confirmed to be the case in acidic solutions by Qiao et al. [15]. Conversely, Tang et al. [16] indicated that the chromium oxide content in L-PBF processed material was surprisingly lower than that of its conventional counterpart, resulting in reduced corrosion resistance of the additively manufactured material. Moreover, authors' previous research demonstrated that even slight adjustments to parameters such as laser power can markedly affect the corrosion and SCC behaviour of L-PBF processed alloy 718 [17].

Another critical aspect relates to the breakdown of the passive layer under tensile loading. Despite significant research comparing additively manufactured materials with their conventional counterparts, the behaviour of the passive layer during breakdown has received little attention. Moreover, few previous studies have focused on corrosion during the propagation stage under tensile loading experiments. Among those studies, Dai et al. [18] reported unstable cracking behaviour of L-PBF 316L due to the influence of loading direction. Santamaria et al. [19] highlighted lower crack propagation resistance in L-PBF materials, attributing it to internal residual stresses. Que et al. [20] indicated better cracking resistance in as-built L-PBF 316L compared to solution-annealed samples, attributed to significantly finer grains. Cabrini et al. [21] studied the stress corrosion cracking of L-PBF 316L under different strain rates and reported almost similar behaviour under low strain rates.

Investigating the initiation and incubation stages of passive layer breakdown which is essential for understanding a material's cracking mechanism and susceptibility to cracking, has been limited by limitations in electrochemical test setups and the difficulties in detecting such highly localized events on the large surface areas typically employed in corrosion studies. Recently, microcapillary electrochemical techniques have provided insights into the initiation of corrosion- and stress-assisted breakdown of the passive layer [17,22–25]. The previous studies by the authors have revealed the role of factors such as local galvanic cell formation near cell boundaries and high dislocation density adjacent to them on surface cracking susceptibility of additively manufactured alloy 718. However, there remains a lack of systematic analysis and high-resolution characterization of passive layer breakdown to acquire a more complete understanding of the corrosion and stress-assisted crack initiation mechanism. To the best of the authors' knowledge, no existing investigation has examined the true nature of passive layer breakdown in additively manufactured Ni-Fe-Cr-based alloy 718 by high resolution analytical techniques.

The current investigation explores the mechanism of passive layer breakdown under corrosion and tensile loading condition for L-PBF processed Ni-Fe-Cr-based alloy 718. This pioneering study utilizes a range of microcapillary electrochemical techniques alongside high-resolution analyses including TEM, EDX, EELS, XPS, and SKPFM. By delving into the underlying mechanisms behind passive layer breakdown and correlating them with observations from microcapillary electrochemical polarization results, the research sheds light on the exceptional breakdown of the passive layer observed in L-PBF fabricated Ni-Fe-Cr-based alloy 718. This alloy is widely employed in critical industries situated in coastal regions prone to chloride ion contamination, making the findings particularly relevant and impactful.

2. Materials and methods

2.1. L-PBF processing and sample preparation

Ni-Fe-Cr-based alloy 718 gas atomized powder (ISO-NiCr19Nb5Mo3) with particle sizes ranging from 10 μm to 55 μm was utilized. Using an EOS M100 laser metal fusion machine equipped with a 200 W fibre laser, specimens measuring 30×10×30 mm were processed. To optimize the L-PBF process parameters for this study, single-track experiments were conducted across a range of parameter combinations. Subsequently, cuboidal specimens measuring 10mm × 10mm were fabricated and their densities determined using the Archimedes method. Microstructural analysis was also performed to evaluate the morphology and distribution of defects within the samples. The optimal L-PBF process parameters were selected based on the highest achieved density and the lowest density of observable porosity. For a more comprehensive understanding of the underlying principles and methodologies, readers are referred to the authors' previous investigation [17].

The optimal combination of process parameters, including a layer thickness of 20 μm, hatch spacing of 70 μm, laser power of 115 W, bidirectional alternating chess scan strategy, and a laser spot diameter of 30 μm, resulted in the highest density achieved in this study. Cuboid samples were then prepared from the additively manufactured specimens in their as-built state through electro-discharge machining (EDM), with dimensions of 10×30×0.8 mm, sliced perpendicular to the build direction. Following precise grinding and polishing up to 0.1 μm alumina suspension, the samples underwent a 15-minute ultrasonic wash in a 30% ethanol solution, followed by rinsing with pure ethanol.

2.2. Material characterization

The microstructure and chemical composition of the surface oxide formed were investigated using a FEI QUANTA 250 field emission scanning electron microscope (FE-SEM) equipped with an Oxford Instruments Energy Dispersive X-ray (EDX) detector system. Site-specific Transmission Electron Microscope (TEM) thin foils were prepared using a dual beam Zeiss NVision 40 Focused Ion Beam (FIB-SEM). Higher resolution analyses on the TEM foils were then performed using a probe aberration-corrected JEOL ARM200F TEM equipped with Jeol 100mm^2 Centurion EDX detector and a Gatan Quantum 965 ER for Electron Energy Loss Spectroscopy (EELS) detector. It was operated at 200kV in STEM mode, using probes with 30 mrad convergence and 40mrad collection half-angles. Two annular detectors were used to produce annular dark field (ADF) images containing diffraction contrast and high-angle ADF (HAADF) images with Z-contrast. EDX and EELS quantitative analysis was standardless and are assumed to contain a 10% relative error.

Scanning Kelvin Probe Force Microscopy (SKPFM) was conducted with a Park Systems XE–100 atomic force microscope. Rectangular conductive cantilevers (ANSCM–PT from AppNano), coated with Pt/Ir, featured resonant frequencies of 50 to 70 kHz and spring constants of 1 to 5 N/m. A dynamic mode with single-pass approach simultaneously captured topography and potential images. The acquired potential signal, termed contact potential difference (CPD), reflected work function differences between probe and surface. Since the external potential signal was applied on the conductive probe, the measured CPD values were inverted to accurately represent Volta-potential values on the sample surface. Sequential SKPFM measurements on specimens were followed by re-measuring the initial sample, ensuring probe Volta potential stability for direct CPD value comparison [26].

X-ray photoelectron spectroscopy (XPS) was conducted using an EnviroESCA spectrometer (Specs) with an AlKα X-ray source (hυ = 1486.6 eV). The analyses were performed under vacuum conditions (approximately 10^{-6} mbar). High-resolution spectra were acquired with a pass energy of 30 eV, integrating for 0.2 seconds per step at 0.1 eV intervals. To address charge accumulation, a binding energy (BE) correction of 284.8 eV was applied for adventitious carbon. XPS spectra were decomposed using Keystone software (Specs) with Shirley-type background subtraction. Quantification parameters were provided by Specs.

2.3. Electrochemical characterization

The microcapillary test method provided an effective means to conduct electrochemical polarization experiments, offering a valuable alternative to traditional techniques for investigating corrosion at a microscale. This method allowed for early-stage observation and analysis of localized corrosion phenomena, such as pitting and SCC, due to its high sensitivity to subtle changes and ability to examine small surface areas. Potentiodynamic, Mott-Schottky polarization experiments were conducted using the microcapillary technique to understand alterations in electrochemical behaviour among specimens in borate buffer solution (H_3BO_3 (0.05 M) + $Na_2B_4O_7.10H_2O$ (0.075 M) with a pH of 9.3). Potentiodynamic polarization measurements were performed from -0.5 to 1.5 V vs. OCP at a scan rate of 1 mV/s. Mott-Schottky polarization measurements were conducted after polarizing samples for one hour at a potential corresponding to the passive region. A potential range of -0.5 to 1 V, a scan rate of -50 mV/s, and an AC amplitude of 10 mV at 1 kHz were used. Electrochemical impedance spectroscopy (EIS) was carried out on a circular area with a 3 mm diameter, covered with strong adhesive tape in borate buffer solution. Frequency range was set between 10 mHz and 100 kHz, with DC amplitude based on Open Circuit Potential (OCP) values and an AC amplitude of 10 mV.

To understand the behaviour of the native oxide layer under tensile loading conditions, specimens were tensile strained at 0.2% strain corresponding to the yield stress of the material. A solution containing 3.5 wt.% sodium chloride in deionized and deaerated water was used to simulate common chloride ion contamination for electrochemical experiments under tensile loading condition for in-depth analysis of possible cracks in passive layer. Experiments under tensile-straining condition were performed using microcapillary technique [25,27], as shown in Figure 1. Potentiostatic electrochemical polarization was carried out by maintaining a constant potential set at breakdown potential obtained from potentiodynamic polarization measurements (obtained in 3.5 % NaCl solution).

The microcapillary contact surface was circular with a diameter of 500 μm, and the tip was sealed with silicon glue to prevent crevice corrosion. The self-isolation nature of the microcapillary method ensured environmental factors did not affect the measured data. All electrochemical measurements were performed using a Gamry Interface 1010E potentiostat unit.
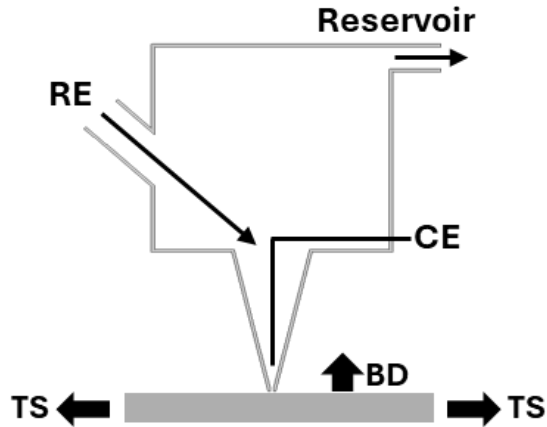
Figure 1. Schematic of microcapillary test setup used for specimens under tensile loading condition. (RE) reference electrode, (CE) platinum wire counter electrode, (TS) direction of tensile straining, and (BD) build direction of L-PBF specimens.

3. Results

3.1. Submicron structure

As depicted in Figure 2, the microstructure of the material exhibits a cellular arrangement with submicron dimensions and intricately decorated cell boundaries. EDX line scans along these boundaries (Figure 2c) revealed an elevated concentration of Nb and Ti at the cell boundaries. This observation aligns with findings reported by Tucho et al. [7–9], suggesting compositional heterogeneity along cell boundaries. While an enrichment in molybdenum (Mo) was observed in the previously mentioned investigation, no significant alteration in Mo content was detected in the current study. A high density of entangled dislocations is also observed near the cell boundaries as shown in Figure 2a. The high density of dislocations is believed to result from the extreme thermal cycles during laser melting and the rapid solidification of each layer, as well as the thermal interaction between successive layers [1–5,28–30]. These dislocations are likely introduced due to the high thermal gradients and the resulting stress fields during the additive manufacturing process.

Additionally, although carbide particles were detected at the nanoscale (EDX analysis not shown herein), their formation was significantly reduced due to the high solidification rates. Such nano scale carbide particles were also detected in authors' previous investigations [17,25]. Carbide formation is typically expected in such alloys, while the rapid cooling rates in the L-PBF process inhibit their nucleation and growth for the case of the current and previous investigations [28,31–33].
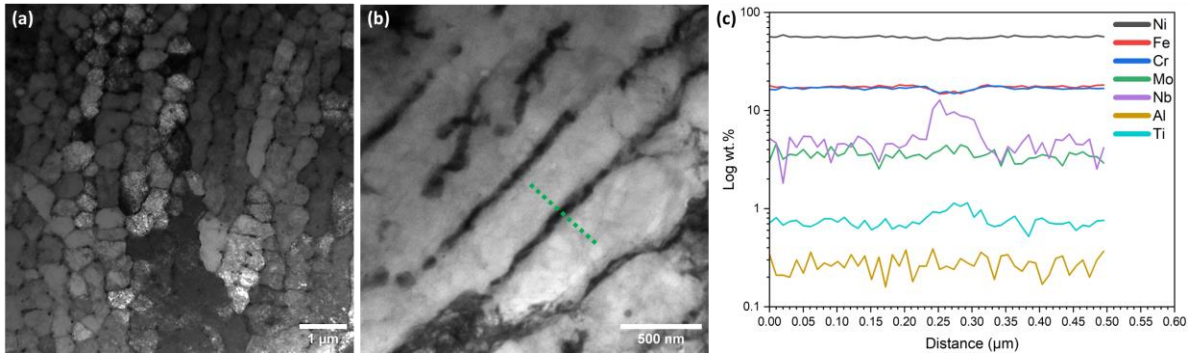
Figure 2. (a) STEM ADF image indicating entangled dislocations, (b) STEM ADF image showing microstructure details and the location of the EDX line profile (green dashed line); (c) corresponding EDX line profile results.

3.2. SKPFM analysis of the native oxide layer

Representative topography and SKPFM maps are shown in Figure 3. While the cellular structure cannot be seen in the topography image (Figure 3a), this is easily identified in the potential map (Figure 3b). As can be seen from the SKPFM maps, the features observed in the potential map (Figure 3b) are independent from those seen in the topography (Figure 3a). While no microstructural characteristic can be recognized in the topography image, the typical cellular structure described in Figure 2 are clearly visible on the Volta potential map. This undoubtedly indicates that no topographical effect has influenced the Volta potential values measured, thus highlighting the reliability of the SKPFM results [34] The borders of the cells can be easily recognized, as the interdendritic region is much thinner than the dimensions of the cells/dendrites. Therefore, the cells borders are the thin regions presenting relatively lower Volta potential values than the inner part of the cells. This can be easily seen in the higher resolution SKPFM potential map presented in Figure 3d, where the interdendritic regions (cells' borders) are highlighted with yellow arrows. The SKPFM line scan analysis on the surface of the polished as-built specimens at various sites, also shown in Figure 3b, and c, highlights lower CPD values at the cell boundaries compared to the cell interiors. This observation is consistent for both melt pool boundaries and melt pool interiors.
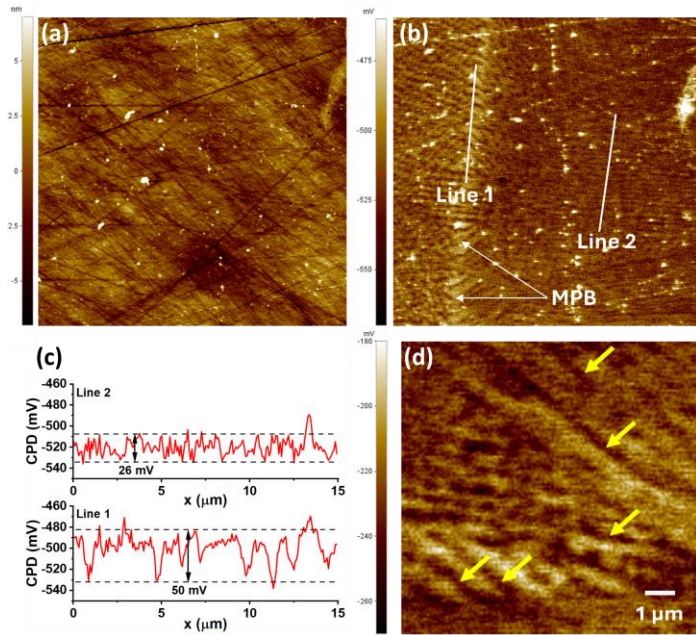
Figure 3. (a) Topography map of the surface, (b) potential (CPD) map, (c) line scan profile corresponding to the shown lines, and (d) higher resolution CPD map at cell boundaries. MPB refers to melt pool border. The scan size is 40×40 μm^2.

However, in the case of melt pool boundaries (line 1 in Figure 3b), the variations in CPD values were more pronounced compared to those within the melt pool interiors. This suggests that the melt pool boundaries experience different elemental micro-segregation conditions compared to the interior of the melt pools, possibly due to the thermal gradients and solidification dynamics at these regions. These results underscore the significant impact of microstructural heterogeneities on the electrochemical properties of the material, as the cell boundaries and melt pool boundaries exhibit distinct electrochemical behaviours.

3.3. XPS analysis of the native oxide layer

XPS analysis of the investigated material's surface, as depicted in the survey XPS analysis of Figure 4, identified several elements including C, O, N, Fe, Ni, Cr, Ti, Nb, and Mo. Carbon and oxygen exhibited the highest surface concentrations among these elements due to the presence of a native oxide layer and adventitious contamination. Detection of nitrogen in XPS spectra is common when analysing metal surfaces, mainly due to interactions during sample handling and preparation. Nitrogen is often used as a purge gas in the XPS exchange chamber to prevent oxidation during transfer, leading to its inadvertent adsorption onto the metal surface. Its strong affinity for metals further contributes to its presence in the spectra,

generating a small but distinct N 1s peak. This peak typically indicates surface contamination from handling or environmental exposure, rather than intentional nitrogen inclusion in the bulk material. The quantitative analysis is summarized in Table 1.
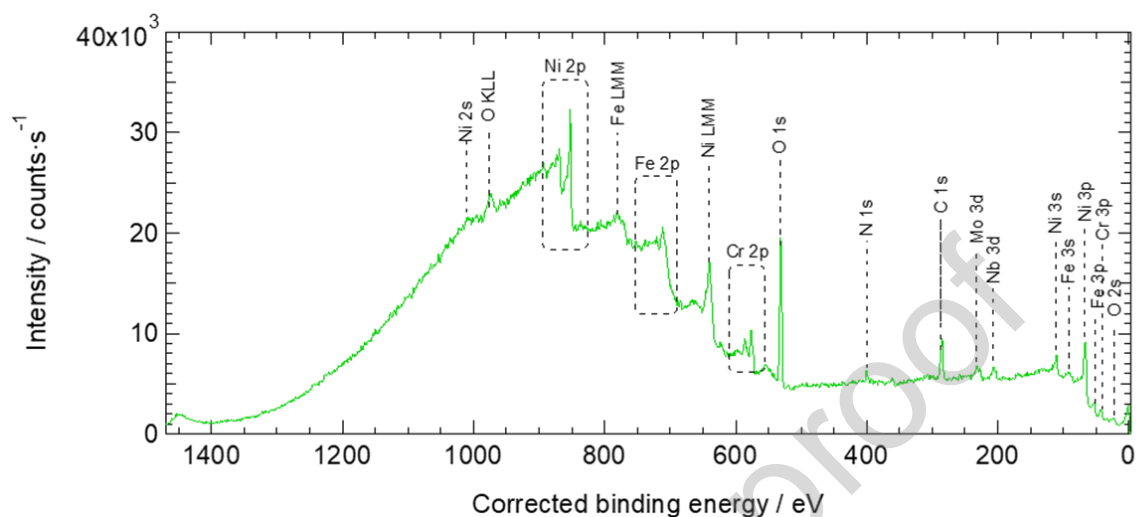

Figure 4. Survey XPS spectra and qualitative analysis of the surface elemental composition.

Table 1. XPS elemental composition of the surface.

Element	C	O	Fe	Ni	Cr	Ti	Nb	Mo	N
at.%	32.06	44.38	1.10	10.20	4.87	0.24	1.32	1.21	4.61

To mitigate the influence of contaminants (e.g., adventitious carbon and adsorbed/chemisorbed oxygen species), the relative composition of surface metals obtained from XPS studies was calculated, and the results are presented in Table 2.

Table 2. XPS relative metal composition of the surface.

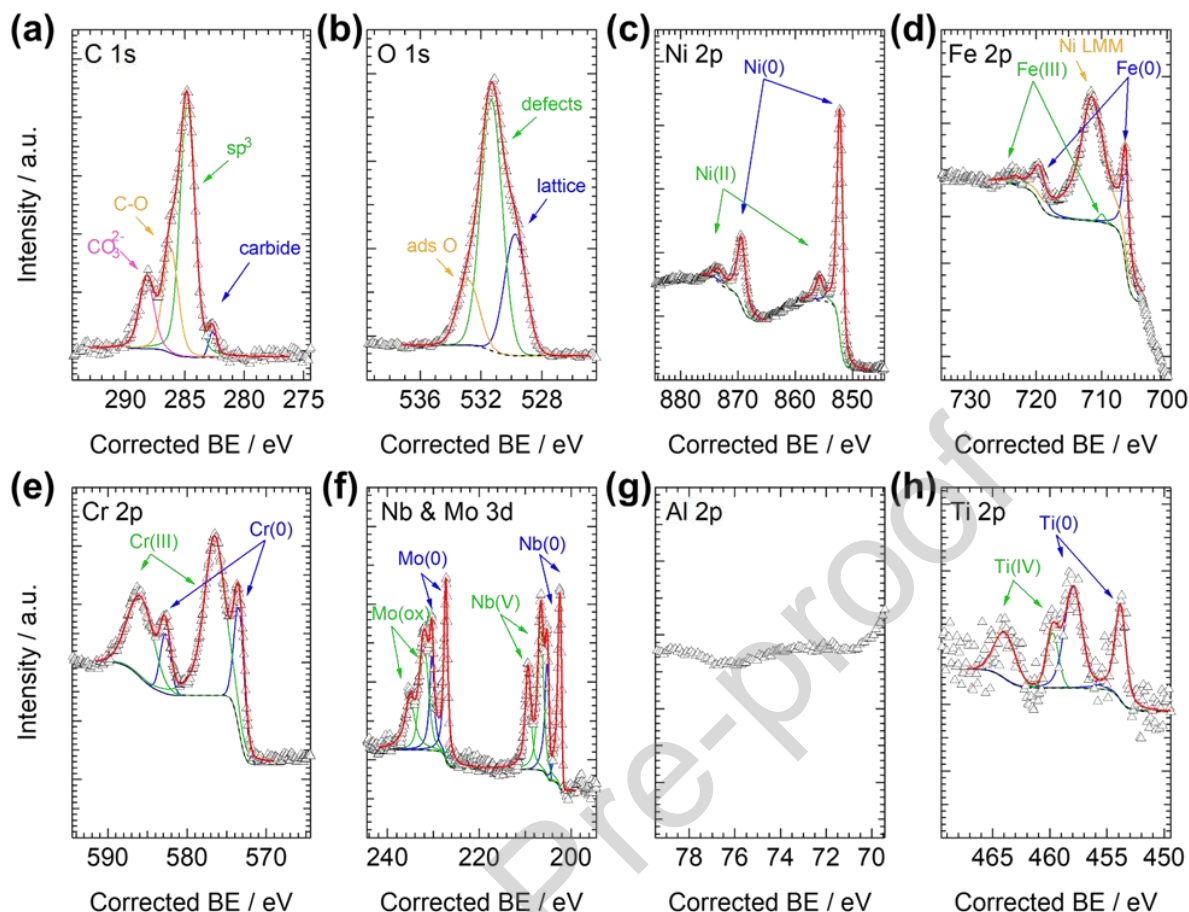| Element	Fe	Ni	Cr	Ti	Nb	Mo
at.%	5.81	53.82	25.72	1.27	6.97	6.41

Figure 5. High resolution XPS analysis and fitting of (a) C 1s, (b) O 1s, (c) Ni 2p, (d) Fe 2p, (e) Cr 2p, (f) Nb and Mo 3d, (g) Al 2p, and (h) Ti 2p.

The surface composition ranks in the order of Ni > Cr > Nb > Mo > Fe > Ti. Notably, the surface composition comprises Fe (5.81 at.%), Ni (53.82 at.%), and Nb (6.97 at.%), Cr (25.72 at.%), Ti (1.27 at.%), and Mo (6.41 at.%).

High-resolution XPS investigations revealed the presence of four distinct carbon species (Figure 5a): (i) minor carbides with a peak at approximately 282.6 eV; (ii) adventitious sp3 carbon at 284.8 eV; (iii) C-O species at approximately 286.2 eV; and (iv) chemisorbed carbonates centred at approximately 288.2 eV. In the O 1s spectral region, three features were consistently observed (Figure 5b): (i) a peak at low binding energies (BEs) of approximately 529.7 eV, associated with lattice oxygen atoms within the metal oxides framework; (ii) a peak at medium BEs of approximately 531.2 eV, corresponding to surface-chemisorbed hydroxyls or carbonates and/or defects in surface metal oxides; and (iii) a peak at high BEs of approximately 532.9 eV, attributed to adsorbed or chemisorbed oxygen species such as O_2 or H_2O.

11

In the metal 2p spectral regions, peaks appeared in pairs due to spin-orbit splitting, resulting in the formation of the 2p3/2 (low BEs) and 2p1/2 (high BEs) features. Similarly, in the metal 3d spectral regions, peaks were split into their 3d5/2 (low BEs) and 3d3/2 (high BEs) features.

In the Ni 2p spectral region (Figure 5c), two distinct nickel species were observed: (i) Ni(0) peaking at approximately 852.2 eV; and (ii) Ni(II) in the form of hydroxides centred at approximately 855.6 eV. Similar to iron, nickel surface atoms were predominantly present in their metallic form. In the Fe 2p spectral region (Figure 5d), two different iron species were detected, with the 2p3/2 peaking at approximately 706.3 and 710.2 eV, respectively. The former peak is attributed to iron in the metallic state (Fe(0)), and the latter to Fe(III) species. The Ni LMM line was also present in this spectral range, indicating the presence of nickel. Although iron was primarily present as Fe(0), oxidized iron species were also detected. The Cr 2p spectral region (Figure 5e) revealed the presence of two chromium species: (i) Cr(0) at approximately 573.4 eV; and (ii) surface chromium as Cr_2O_3 at approximately 576.4 eV. Chromium was predominantly present in its oxidized form.

In the Nb 3d spectral region (Figure 5f), two distinct niobium species were observed: (i) Nb(0) peaking at approximately 202.4 eV; and (ii) Nb(V) centred at approximately 206.6 eV. Finally, in the Mo 3d spectral region (Figure 5f), molybdenum species were detected as follows: (i) Mo(0) at approximately 227.2 eV; and (ii) oxidized Mo species (such as Mo IV, V, or VI) at approximately 231.9 eV. Molybdenum exhibited a similar behaviour to niobium, with a comparable ratio between metallic and oxidized forms. Notably, no surface aluminium species were detected in the samples (Figure 5g). In the Ti 2p spectral region (Figure 5h), two different titanium species were detected: (i) the 2p3/2 peaking at approximately 453.8 eV, assigned to titanium in its metallic state (Ti(0)); and (ii) Ti(IV) species at approximately 458.0 eV. Titanium was mainly present as TiO_2.

The relative intensity of the different oxidation states of surface metals obtained from high resolution XPS analysis is summarized in Table 3. The predominant oxide present on the surface of the L-PBF 718 alloy was Cr(III), with lesser amounts were found Fe(III) and Ni(II).

Table 3. XPS relative intensities (in %) and surface composition (at. %) of the different oxidation states of surface metals atoms.

Element	Fe		Ni		Cr		Ti		Nb		Mo	
Oxidation state	Fe(0)	Fe(III)	Ni(0)	Ni(II)	Cr(0)	Cr(III)	Ti(0)	Ti(IV)	Nb(0)	Nb(V)	Mo(0)	Mo(ox)

Relative Intensity (%)	92.15	7.85	87.3	12.7	23.01	76.99	40.38	59.62	42.25	57.75	46.92	53.08
Relative Surface Composition (at. %)	5.35	0.46	46.99	6.83	5.92	19.80	0.51	0.76	2.94	4.02	3.01	3.40

3.4. Electrochemical analysis of passive layer in contact with electrolyte

SKPFM and XPS analyses elucidated the characteristics of the native oxide layer present on the surface of the L-PBF 718 alloy. However, further analysis is required to understand the behaviour of the surface in contact with electrolyte and the passivity of the surface layer.

The results of EIS performed in a borate buffer solution are illustrated in Figure 6. The EIS results reveal the characteristics of the passive layer on the surface when measurements are carried out at the OCP, which has a value of -141 mV relative to the SCE. As depicted in Figure 6a, the Bode plots exhibit dominant capacitive behaviour at medium to low frequencies. This capacitive behaviour is primarily attributed to the passive oxide layer, which provides significant charge transfer resistance against faradaic reactions. The Bode plots further indicate a single time constant for both alloys, signifying capacitive behaviour that is closely associated with the characteristics of the passive layer. The electrochemical impedance measured at higher frequencies is generally linked to the resistance of the electrolyte in contact with the electrode.
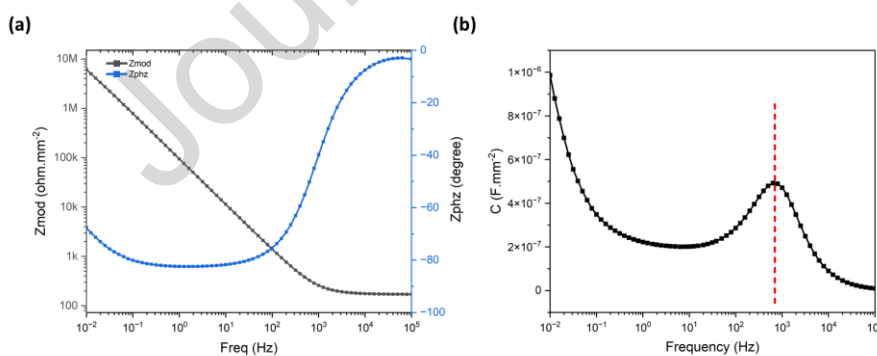

Figure 6. (a) Bode and phase angle for EIS measurements in borate buffer solution at OCP value with respect to SCE, and (b) capacitance behaviour over the frequency range.

Examination of capacitance variation obtained from the EIS findings (Figure 6b) suggests that a frequency of 1 kHz could be optimal for distinguishing the predominant influence of space charge capacitance over double layer capacitance for further analysis of the semiconducting

13

behaviour of the LPBF-718 alloy through Mott-Schottky analysis. The determination of interfacial capacitance (C) involves the use of the system software of the potentiostat (Gamry Echem2 Analyst), employing the relation $C=(-Z''2\pi f)^{-1}$, where Z'' represents the imaginary part of the impedance and f is the frequency.

Furthermore, Figure 7 presents the association of Mott-Schottky analysis with potentiodynamic polarization outcomes performed in borate buffer solution in order to gain further insights regarding the passive layer and its semiconducting nature. Notably, the potentiodynamic polarization results indicate a broad passive state range for the specimen, signifying the development of a passive layer during polarization experiments. At -693 mV$_{SCE}$, the current density began to decrease as the potential increased, reaching a minimum value at -517 mV$_{SCE}$.
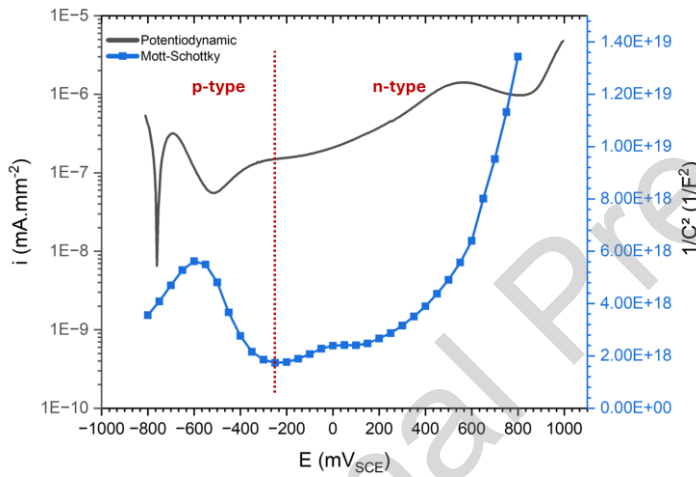

Figure 7. Microcapillary potentiodynamic and Mott-Schottky polarization analysis in borate buffer solution.

As the potential difference continued to increase, the current density experienced a slight rise but remained relatively stable until the breakdown point was reached. At a breakdown potential of 832 mV$_{SCE}$, the passive layer could no longer maintain its integrity, resulting in its breakdown. At this point, the release of metal ions was facilitated, leading to a higher detected current density at potential differences beyond the breakdown point. This behaviour highlights the efficacy of the chromium-enriched passive layer in providing corrosion resistance by limiting ion mobility. However, once the passive layer is compromised at the breakdown potential, the protective effect is lost, and increased corrosion occurs due to the enhanced release of metal ions.

The Mott-Schottky analysis shown in Figure 7 (focusing on the passive range from -693 to 832 mV$_{SCE}$), depicts a negative slope indicative of p-type behaviour, particularly near the low

14

potentials of the potentiodynamic polarization curve (anodic branch). The p-type region of Figure 7, corresponds to a potential range where passivity dictates the rate of anodic reactions at the outer layer/solution interface. As the potential increases, the capacitance also increases, reaching its maximum value at -288 mV$_{SCE}$. Beyond this potential, the capacitance begins to decrease, indicating the characteristics of an n-type semiconductor with a positive slope in the $1/C^2$ vs E plot. At higher potentials, where metallic ion dissolution intensifies, the space charge capacitance of the passive layer reduces, reflecting an n-type behaviour with steeper slope. This transition is attributed to the compromised resistance of the passive layer against electron flow, caused by the potential difference between the working electrode (the specimen) and the counter platinum wire. At potentials higher than -288 mV$_{SCE}$ (n-type region with positive slope), the capacitance analysis and its gradual decrease, predominantly explores the outer layer, believed to consist of nickel and iron oxides and hydroxides that are ejected through the chromium oxide inner barrier layer [35].

The interaction of the passive layer in a borate buffer solution has been studied to elucidate the formation and integrity of the passive layer across a wide range of potential differences applied between the specimen and the counter electrode. This investigation has clarified how the integrity of the passive layer varies with increasing potential and identified the potential at which degradation of the passive layer begins. The behaviour of the L-PBF processed alloy 718 in both the as-built and tensile-loaded states was thoroughly reported in the authors' previous investigations [17,25]. However, to further reveal the occurrence of breakdown for high-resolution analytical analysis in cross-section, additional studies were conducted under tensile loading in an aqueous solution contaminated with chloride, which is the most common contaminant, considering the application of Ni-Cr-based alloys in critical industries located in coastal regions.

3.5. Electrochemical analysis of passive layer breakdown under tensile loading

Microcapillary potentiostatic polarization experiments were conducted under tensile straining equivalent to a 0.2% proof strain in a 3.5% sodium chloride aqueous solution. The applied potential corresponded to the critical value determined from potentiodynamic polarization measurements at breakdown point, marking the onset of passive layer breakdown [17,23,25]. The objective of this approach is to identify the moment when breakdown initiates, facilitating further examination of the initial stages of passive layer degradation with high resolution microstructural techniques used in the current investigation.
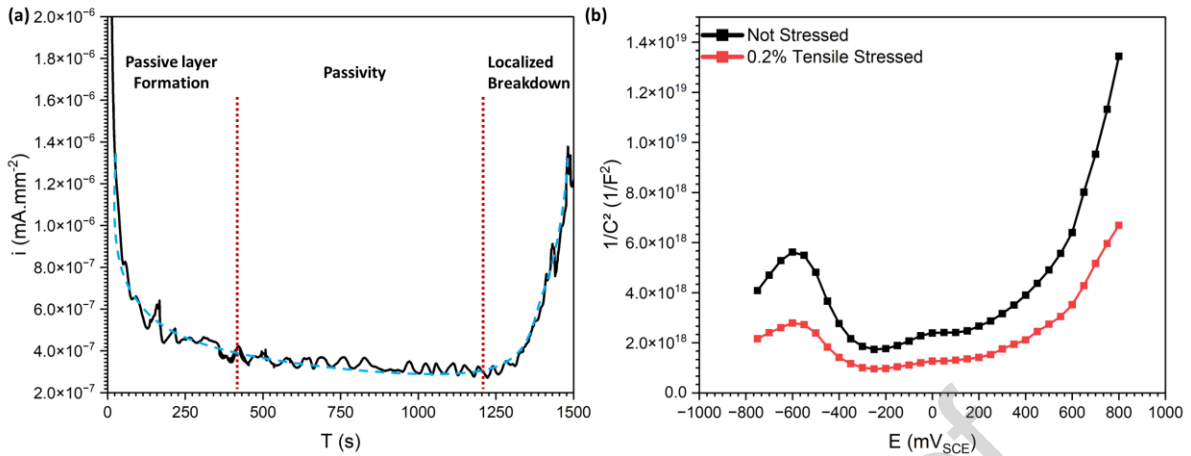
15

Figure 8. Microcapillary (a) Potentiostatic polarization performed in 3.5% sodium chloride solution at breakdown potential, highlighting various stages of passive layer formation and annihilation, and (b) Mott-Schottky analysis on with and without applying tensile stress in borate buffer solution.

During the initial stages of potentiostatic polarization (Figure 8a), the current density substantially decreases, indicating the formation of a barrier layer that hinders the release of ions, corresponding to the lower detected current density. This decrease in current density suggests the formation of a passive chromium oxide layer on the surface. After approximately 420 seconds, the current density reaches a steady state. The sustained low current density until approximately 1225 seconds indicates the presence of a stable barrier layer on the surface, effectively resisting the ejection of metal ions. When the passive layer is intact, minimal current passes through due to its resistive properties.

However, after approximately 1225 seconds, a significant increase in current density is observed, indicating sustained corrosion of the specimen. This sudden increase in current density indicates the diminished resistance of the surface barrier layer, allowing the movement of ions and facilitating the ejection of metal ions through the passive layer. This marks the initial stages of passive layer breakdown. Upon breakdown and subsequent ion release, current levels increase significantly. It is worth mentioning that the potential reflects the difference between the platinum wire and the working electrode, serving as an estimation for potential fluctuations at the metal-solution interface, influenced by its resistance-capacitance dynamics. The occurrence of corrosion at notably higher current density signifies the degradation of the passive layer and higher flux of ions at metal/solution interface.

Furthermore, microcapillary Mott-Schottky analysis conducted on specimens with and without tensile straining in borate buffer solution reveals significant changes in capacitance and charge

16

carrier density, as illustrated in Figure 8b. After applying tensile strain to the sample, the number of charge carriers, which is inversely proportional to the slope of the straight line, increased markedly for both the inner Cr oxide (p-type region with a negative slope) and the outer Fe/Ni oxide (n-type region with a positive slope). This observation underscores the influence of the material's internal energy state on defect density. It should be emphasized that the charge carriers in passive layers consist of anion vacancies, cation vacancies, and cation interstitials, all of which are considered crystallographic point defects within these layers.

Additionally, an increase in the overall space charge capacitance of the material was observed after tensile straining, highlighted by the shift of the tensile strain curve to lower values. This shift indicates that tensile straining not only affects the defect density but also enhances the space charge capacitance, further impacting the electrochemical behaviour of the passive layer. These findings emphasize the critical role of mechanical stress in altering the passive layer's properties and its implications for the corrosion resistance of the alloy.

3.6. High resolution analysis of passive layer breakdown after stress-assisted corrosion

Figure 9 shows the surface of the specimen after the stress-assisted polarization experiments after the detection of sudden increase in current density, and the corresponding location where the FIB milling was performed for further TEM analysis.
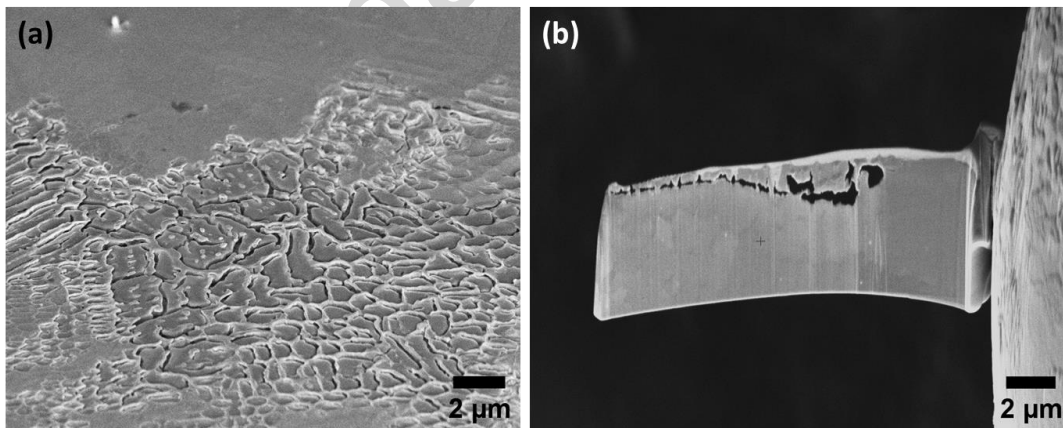

Figure 9. (a) Secondary electron micrograph showing the surface after stress-assisted microcapillary polarization, and (b) FIB prepared cross-sectional TEM foil prepared from that region showing the breakdown of the passive layer.

Submicron cracks were clearly observed at sites adjacent to cell boundaries. The mechanism for the formation of these cracks on passive layer at such specific locations has been thoroughly elucidated in the authors' previous investigations [17,25]. It is proposed that the combined

effects of a coupled environment and a high density of entangled dislocations are the primary factors promoting the formation of surface cracks near the cell boundaries. However, in this study, we explore for the first time the initial stages of passive layer breakdown and cracking behaviour normal to the surface of the specimen (through high-resolution analysis of the surface in cross-section).
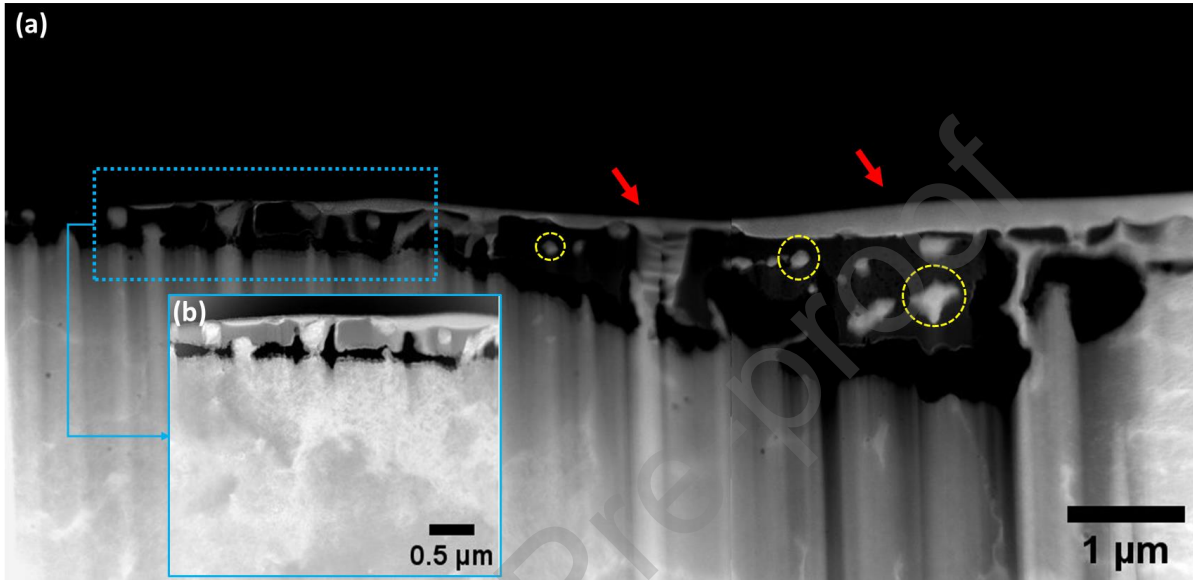

Figure 10. (a) HAADF image of the cross-section of the passive layer with protective Pt coating shown with red arrows, presence of not oxidized metallic particles within the oxide layer shown with yellow circles, and annular dark-field (ADF) image with higher magnification shown in blue (b), indicating high density of dislocations adjacent to surface.

To protect the passive layer during the FIB milling process, the surface was coated with a layer of platinum. STEM high-angle annular dark-field (HAADF) images, as displayed in Figure 10, show a thick oxide layer on the surface where EDX and EELS analyses were conducted. An important finding observed across multiple locations, beyond the illustrated images, was the presence of voids underneath the oxide layer and the separation of the passive layer from the metal surface beneath.

Under the tensile loading conditions of this study, small sharp edges were also identified on the base material, potentially serving as initial points for surface crack for possible propagation. Metallic particles that had not oxidized, located at cell boundaries and partially embedded in the surface oxide layer, are clearly visible in the HAADF images shown in Figure 10 with yellow circles. Angular dark field (ADF) image shown in blue in Figure 10 reveals a high density of dislocations close to the metal/oxide interface.

Additional EDX line scan analysis conducted within the passive layer (illustrated in Figure 11) unveiled oxides enriched with Nb and Mo, alongside minor quantities of Ti, Cr, and Fe. Conversely, the non-corroded cell boundaries exhibited a higher percentage of Ni, Cr, Nb, and Fe. The primary surface oxide appears to be rich in niobium and molybdenum, with a composition of $(Nb_{0.64}Mo_{0.36})O_2$. In addition to niobium and molybdenum, this oxide layer contains small amounts of titanium, chromium, and iron. EDX mapping of the cross-section, as depicted in Figure 12, revealed nearly identical levels of Al, Si, and Ti, while the oxide layer exhibited notably lower levels of Ni, Cr, and Fe.
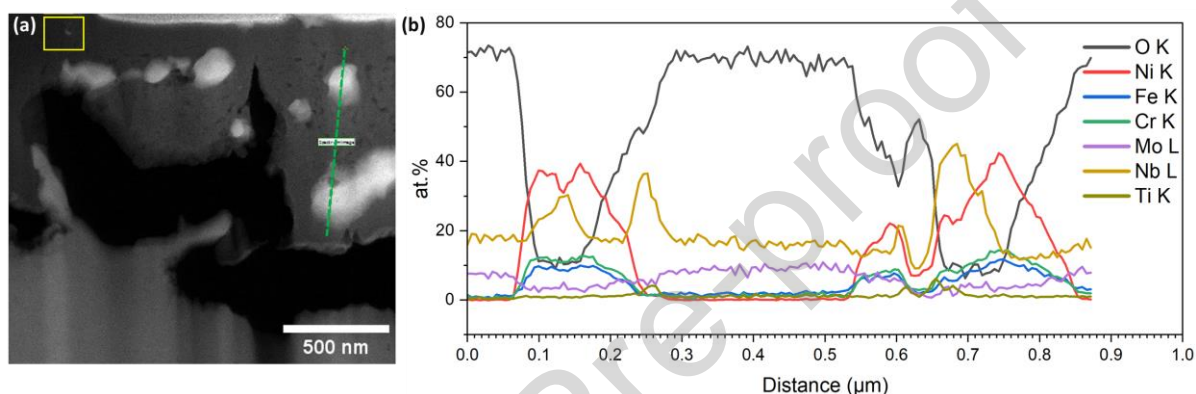

Figure 11. (a) HAADF image indicating the location of the EDX line profile across the surface oxide layer (green dashed line) with the region used for drift correction indicated by the yellow box. (b) EDX line profile.

Further compositional maps obtained by EDX and EELS are shown in Figure 12. The EELS analysis (Figure 12) clearly shows a thin oxide layer on the metal part beneath the detached and cracked thicker oxide. The oxygen diffusion results in a reduced chromium content in these regions. The presence of oxygen in this layer suggests that the metal is undergoing oxidation, which can weaken the protective oxide layer by depleting the chromium that is essential for maintaining its integrity. This reduction in chromium content could compromise the corrosion resistance of the material, making it more susceptible to further degradation.
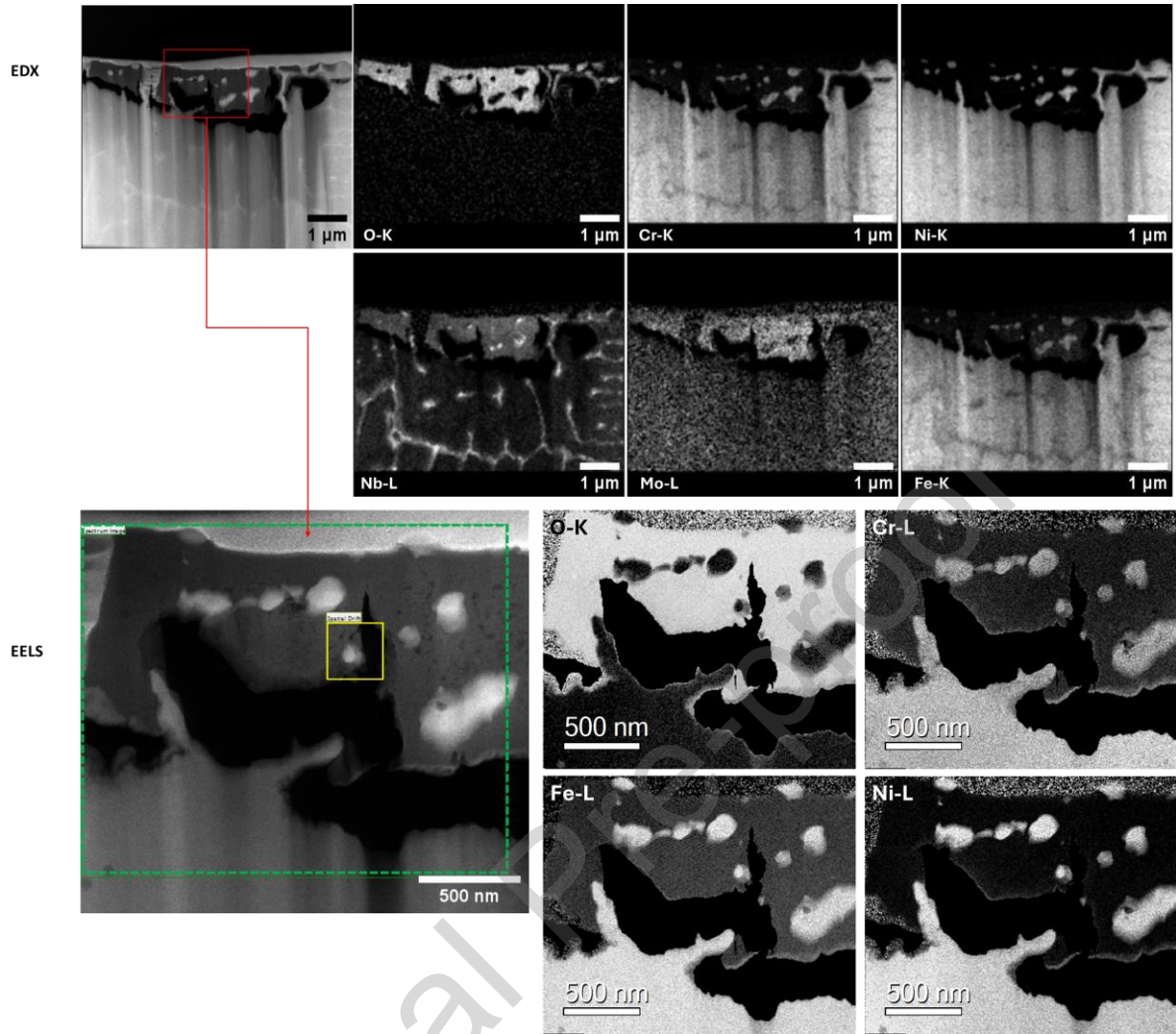
19

Figure 12. HAADF images and corresponding EDX and EELS elemental maps from the cross-section of the passive layer.

Quantitative EDX analysis of the non-oxidized cell boundaries, as shown in Figure 13, and summarized in Table 4, indicates that the structure is rich in Cr, Fe, Ni, Nb, and Mo. In contrast, the oxide contains significantly less Cr, Fe, and Ni, but higher levels of Mo and Nb, as also seen in the EELS elemental map of Figure 12. For context, the composition of the matrix remains within the typical specifications for this alloy, comprising 18 wt.% Cr, 6 wt.% Nb, and 4.45 wt.% Mo.
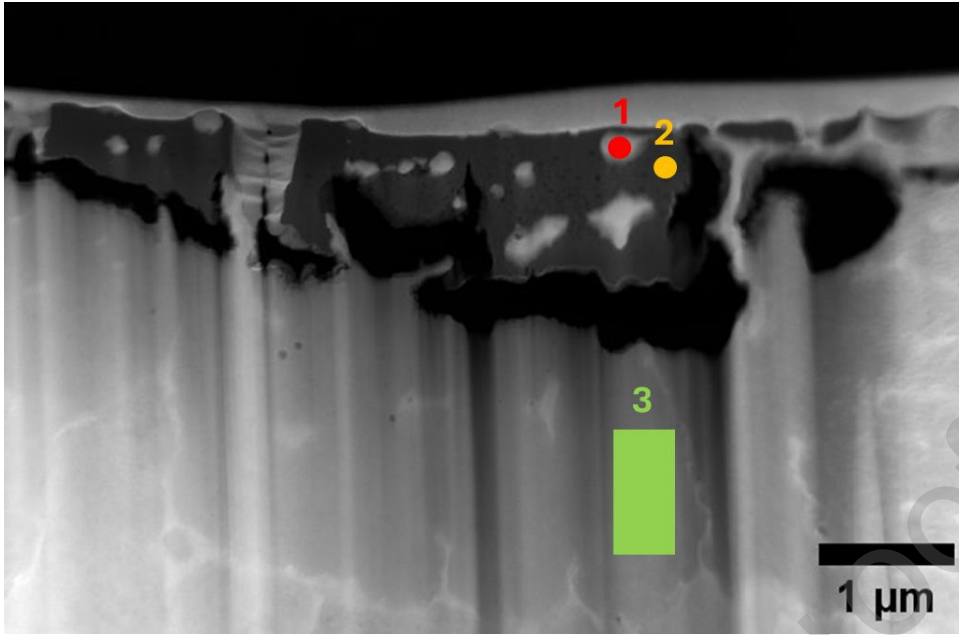
20

Figure 13. HAADF image showing the regions used for quantitative EDX analysis.

Table 4. Quantitative EDX-TEM analysis of the regions shown in Figure 13 considering 5% of error.

Element (Wt.%)	Region (1)	Region (2)	Region (3)
O K	6	41	-
Al K	0.7	0.2	0.7
Ti K	1.9	2.2	0.7
Cr K	12	3	18
Fe K	9.7	5.7	17
Ni K	37	1.7	51
Nb L	27	28.5	6.1
Mo L	5.2	16.4	4.4

4. Discussion

In a previous study [25], the authors compared the L-PBF processed alloy 718 with its conventionally produced counterpart, focusing on electrochemical polarization behaviour and structural differences. The results indicated that conventionally produced alloy 718 exhibited significantly larger crack initiation compared to the AM variant. Employing various microcapillary electrochemical techniques, the authors confirmed the superior corrosion performance of the L-PBF processed alloy 718. Additionally, a mechanism for the breakdown of the passive layer under tensile loading conditions was proposed for the L-PBF processed alloy. The significantly smaller grain size, reduced presence of MC and $M_{23}C_6$ carbides, and absence of phases commonly found in conventional alloy 718 (γ'-Ni_3(Al,Ti), γ''-Ni_3Nb, and

21

needle-shaped δ-Ni$_3$Nb) were identified as key factors contributing to the improved corrosion resistance and passive layer breakdown.

It is well established that oxide layers on Ni-Fe-Cr-based alloys consist of an inner Cr-based oxide layer, which provides the primary passive behaviour, and an outer layer of Ni-Fe-based oxides and hydroxides [36–41]. The oxidation of multicomponent alloys, such as stainless steels and nickel-based alloys, is a complex process influenced by both thermodynamic stability and atomic diffusion. As extensively documented in the literature [42], chromium's strong affinity for oxygen and favourable oxidation kinetics lead to the preferential formation of a continuous, protective Cr$_2$O$_3$ layer. This oxide layer acts as a barrier, hindering further oxidation of the underlying alloying elements. The inner Cr$_2$O$_3$ layer and the outer layer, primarily composed of nickel and iron oxides or hydroxides [35,41,43,44], are influenced by factors such as oxygen partial pressure, temperature, and alloy composition.

At relatively higher potentials, the point defect model [37,38] postulates that nickel and iron may be ejected from the chromium oxide layer at the metal/passive layer interface. However, the kinetics of passive layer formation and performance can be affected by compositional [45] and microstructural variations arising from changes in additive manufacturing process parameters [17,25]. Further in-depth studies are required to fully understand the impact of these factors on the overall corrosion behaviour of additively manufactured alloys.

Furthermore, the observed capacitive behaviour and the single time constant in the EIS data suggest that the passive layer is highly effective in inhibiting charge transfer processes, in a good agreement with XPS results indicating the dominant presence of Cr(III) oxides on the surface. On the other hand, the Cr$_2$O$_3$ layer is widely recognized as a p-type semiconducting layer with a negative slope in Mott-Schottky analysis within the passive region [35,40,41,43,44,46–48]. This negative slope indicates a predominance of metal cation vacancies in the film, suggesting that the growth of the film and the formation of a new oxide layer are controlled by the movement and annihilation of these vacancies at the metal-film interface. Provided that the rate of oxidation reactions leading to the formation or thickening of the passive layer exceeds the rate of dissolution reactions, the material exhibits a barrier against significant ion dissolution. As previously illustrated in Figure 8a, during the initial stages of polarization, the decreasing current density over time reflects a reduction in the oxidation rate as the film thickness increases until reaching a steady state, where it becomes independent of polarization duration. The Steady state current density observed in Figure 8a

22

suggests that the dissolution rate is not influenced by film thickness. The Cr_2O_3 layer formed on the surface acts as a diffusion barrier, restricting the free movement of ions. The sustained low current density observed during potentiostatic polarization measurements over a wide potential range indicates the presence of such a barrier layer. According to Ohm's law, at a constant applied potential, current density is inversely proportional to resistance. Therefore, the significantly lower current density measured during the passive state, as shown in Figure 8a, suggests the presence of a barrier to the free movement of ions between the working electrode and the counter electrode. Moreover, the sudden increase in current density after a certain polarization time clearly indicates a breakdown of the passive layer's resistivity, allowing for the free transfer of ions through the compromised layer.

4.1. Electrochemical polarization response and passive layer breakdown

The subsequent phase of this investigation was dedicated to gaining a thorough understanding of the mechanisms underlying the degradation and breakdown of the passive layer when subjected to stress-assisted corrosion. The application of external stress to the material can cause significant microstructural alterations, such as changes in the distribution and magnitude of dislocation densities, which can in turn influence the formation and/or degradation of the passive oxide film. High resolution in-situ microstructural analysis during tensile loading may provide further insights into the relationship between dislocations during tensile loading and oxide film formation and/or degradation. Conducting such in-situ analyses to investigate submicron alterations in additively manufactured materials represents an interesting avenue for future research.

Through Mott-Schottky analysis, the semiconducting behaviour of the passive layer was examined as a function of potential difference. Contrary to common belief, which suggests that the breakdown of the passive layer occurs at a specific breakdown point (observed at high potentials in potentiodynamic polarization curves where a sudden increase in current density is detected), degradation of the passive layer begins well before reaching this point. A gradual decrease in capacitance (as depicted in the n-type region of the Schottky barrier in Figure 7) clearly indicates the progressive degradation of the passive layer with increasing potential.

The resistive and semiconductive properties of the passive layer were analysed over a range of potentials within the passive region, as previously illustrated in Figure 7. The results clearly demonstrate that while the passive layer offers resistance toward the free movement of ions between the specimen and the platinum counter electrode, evidenced by minor variations in

23

current density during potentiodynamic polarization, increasing the potential within the passive range induces a noticeable change in the slope of the n-type region of the Mott-Schottky curve shown in Figure 7. This slope is inversely proportional to the density of charge carriers, implying that a steeper slope at higher potentials corresponds to a lower charge carrier density [49]. Mott-Schottky theory further indicates that the width of the depletion region is inversely related to the square root of the charge carrier density, suggesting that a steeper slope indicates a wider depletion region.

Over the past decade, it has been well-established that the n-type behaviour observed in austenitic stainless steels and Ni-Fe-Cr-based superalloys is associated with the formation of outer Ni-Fe-enriched oxides/hydroxides [35,39–41,44,46,48,50]. Consequently, it is reasonable to conclude that the increased thickness of the passive film, as indicated by a wider depletion region, is directly related to the growth of the outer Ni/Fe-enriched layer. Since the formation of a thicker outer layer suggests an easier ejection of Ni and Fe ions from the protective inner Cr_2O_3 barrier, it can be presumed that higher potentials facilitate this ejection, leading to a thicker, more porous outer layer. On the other hand, according to the Point Defect Model [38,51], the flux of oxygen vacancies and/or cation interstitials (Cr^{2+}, Cr^{3+}, Fe^{2+}, and Ni^{2+}) through the passive film is essential for its growth. However, it is important to emphasize that the outer Ni/Fe-enriched oxide/hydroxide layer does not contribute to the protective properties of the passive layer, which are primarily attributed to the inner Cr_2O_3 layer.

Given that both oxidation and dissolution reactions occur under polarization conditions, it is necessary to elucidate the mechanism responsible for the logarithmic increase in the dissolution rate at the breakdown potential observed previously in Figure 8a. The point defect model proposed by Macdonald et al. [37,38,51] suggests that transpassive dissolution involves the generation of cation vacancies at the outer layer of the film, leading to a thick and porous surface film. These defects are crucial for ion transport through the passive film and migrate through the film under the influence of electric fields and concentration gradients. When the flux of cation vacancies surpasses the rate at which they can be annihilated at the interfaces, they accumulate within the passive film. This accumulation leads to the condensation of cation vacancies into voids, generating a porous structure within the passive film. As the concentration of cation vacancies increases, the integrity of the barrier layer diminishes, eventually forming critical flaws or weakened regions in the passive film. These critical flaws are particularly susceptible to breakdown, especially in the presence of higher energy states, thereby initiating localized corrosion processes.

Additional evidence supporting the impact of internal stresses comes from the microcapillary Mott-Schottky analysis conducted on specimens under tensile strained state, as shown in Figure 8b. The observed increase in charge carrier densities for the tensile strained specimen compared to as-built state for both n-type and p-type regions indicates the presence of a more defective passive layer on the surface (gentle slope). It is well recognized that lower density of charge carriers inhibits ion migration, which subsequently restricts electrochemical and chemical reactions within the passive film. A lower carrier density makes it more difficult for ions to diffuse through the passive film [35,40,41,43,46–48,52].

The final part of the current investigation, which to the best of the authors' knowledge is being explored for the first time and constitutes the primary novelty of this research, focuses on elucidating the principal mechanism of passive layer breakdown in L-PBF processed Ni-Fe-Cr-based alloys and the morphology of corrosion attack leading to passive layer degradation under tensile loading conditions. The results revealed the presence of voids at the interface between the oxide layer and the bare metal surface. Additionally, cracks were clearly observed in the passive layer adjacent to cell boundaries. To fully understand the underlying mechanisms, several factors must be considered, as discussed below.

4.2. Correlation of surface Volta-potential with occurrence of passive layer breakdown

The compositional EDX analysis (shown in Figure 2) at the cell boundaries highlights clear compositional heterogeneity between the cell interiors and boundaries. Specifically, slightly lower concentrations of Ni, Fe, and Cr are detected at the cell boundaries, also reported by other authors [7–9]. On the other hand, high-resolution SKPFM analysis (see Figure 3) further indicates lower CPD values at the cell boundaries compared to the cell interiors. Classical interpretations of these results [53,54] might suggest that cell boundaries have lower corrosion resistance compared to cell interiors. However, based on the findings from the current investigation, it is evident that cell interiors are more prone to corrosion, as has also been reported by numerous authors for austenitic stainless steels and other Ni-based alloys [55–57]. This seemingly contradictory trend between the Volta-potential and the corrosion susceptibility of the cells' interior in relation to the cells' borders can be due to local differences in the passive oxide layer thickness. On the cells' interior, a relatively thicker oxide can be formed, rendering the Volta-potential measured for these regions higher than the potentials measured at the cells' borders, despite the fact that the cells' interior presents a higher susceptibility to passive layer breakdown. Moreover, unusual correlations between local SKPFM data and corrosion

susceptibility of different phases have also been reported in previous studies for other Ni-based alloys [58].

This observation highlights the fact that the internal energy state at the submicron level significantly impacts corrosion behaviour and performance. It is well recognized that dislocations act as fast diffusion paths and in a recent investigation by Lozano-Perez et al. [59] on high-resolution analysis of native oxide layers on austenitic stainless steels, the diffusion of oxygen and the ejection of metallic ions were confirmed to be facilitated by the presence of high dislocation density. As a result, in areas with a high density of dislocations in L-PBF processed Ni-Fe-Cr-based alloy 718, the outward diffusion of alloying elements like Ni and Fe (which have less contribution to the corrosion resistance of Ni-Fe-Cr based alloys) is facilitated from the protective chromium oxide inner passive layer confirmed also in authors recent investigation [45].

Consequently, the interior of the cells experiences a greater ejection of Ni and Fe ions, leading to the formation of a thicker outer layer of Ni/Fe oxides/hydroxides. In contrast, at the cell boundaries, the thickness of the outer layer is lower. This is attributed to a lower energy state at these sites, characterized by a reduced density of dislocations and compositional heterogeneity. As demonstrated by the EDS-TEM analysis presented in Figure 2c of this manuscript, L-PBF processed alloy 718 exhibits a higher concentration of Nb and Mo at the cell boundaries, while the Fe and Ni content is lower confirmed also by other researchers for L-PBF processed alloy 718 [7–9]. The combination of a lower energy state and reduced availability of Ni and Fe for oxide/hydroxide formation results in the development of a thinner outer passive layer at these boundaries. Given that the CPD value is sensitive to the thickness of the oxide layer formed on the surface, it is reasonable to infer that the lower CPD value observed at the cell boundaries corresponds to the reduced thickness of the outer Ni/Fe-enriched oxide/hydroxide layer. It is essential to emphasize that the increased thickness of the outer Ni/Fe layer does not necessarily enhance the performance of the passive layer. This is because it is well-established that the inner Cr-enriched oxide layer is primarily responsible for giving the passive characteristics to stainless steels and nickel-based super alloys.

4.3. Passive layer breakdown and corrosion morphology under tensile stresses

Another key observation in the current investigation was the presence of voids beneath the oxide layer, as shown previously in Figure 10, Figure 11, and Figure 12. It is important to note that although FIB milling could potentially enhance the detachment of the passive layer from

the bare metal, the authors confirm the presence of a high density of voids between the oxide layer and the bare metal surface even before FIB thinning of the cross-sectional specimens. As demonstrated earlier in HAADF images of the cross-section (shown in Figure 10, and Figure 13), the breakdown of the passive layer occurred adjacent to the cell boundaries, evidenced by the Pt coating penetrating within the oxide layer. Furthermore, the presence of external tensile stresses promotes the mechanical rupture of the passive layer. This breakdown of the passive layer likely facilitates the contact of the bare metal surface with the solution, creating conditions favourable to ongoing corrosion at sites with higher dislocation density on the surface of the specimen, as indicated by the ADF images in Figure 10.

High-resolution TEM Analysis confirmed that the occurrence of crevice corrosion beneath the oxide layer is highly probable in this scenario. Crevice corrosion can progress beneath the surface due to the accumulation of aggressive ions and a significant decrease in pH levels at localized sites, resulting from reactions between hydrogen and absorbed chloride ions [60]. This observation underscores the importance of understanding the integrity of the passive layer and the underlying metal-oxide interface.

Additional evidence supporting this reasoning is provided by the EELS maps, which are more effective than EDX maps in showing oxygen diffusion due to their higher collection efficiency. A corresponding reduction in chromium content near the interface between the bare metal and the solution (within the void) is also illustrated in Figure 12. These observations indicate that oxygen penetrated into the thin layer of bare metal beneath the oxide layer, leading to localized reduction in chromium content. This process is worsened by the more aggressive environment inside the crevice, which significantly enhances metal dissolution. This issue is particularly critical at sites with high dislocation density, where the metal-oxide interface may be more susceptible to oxidative attack. Consequently, corrosion could extend deeper into the metal near cell boundaries. These areas could then serve as initiation points for stress corrosion cracks, which might propagate throughout the material. In fact, crack tips were clearly observed in Figure 10 on the bare metal underneath the detached oxide layer (next to a cell border). Figure 14 provides a schematic illustration of the previously explained mechanisms, summarising the synergistic effects of various factors discussed in the current investigation.
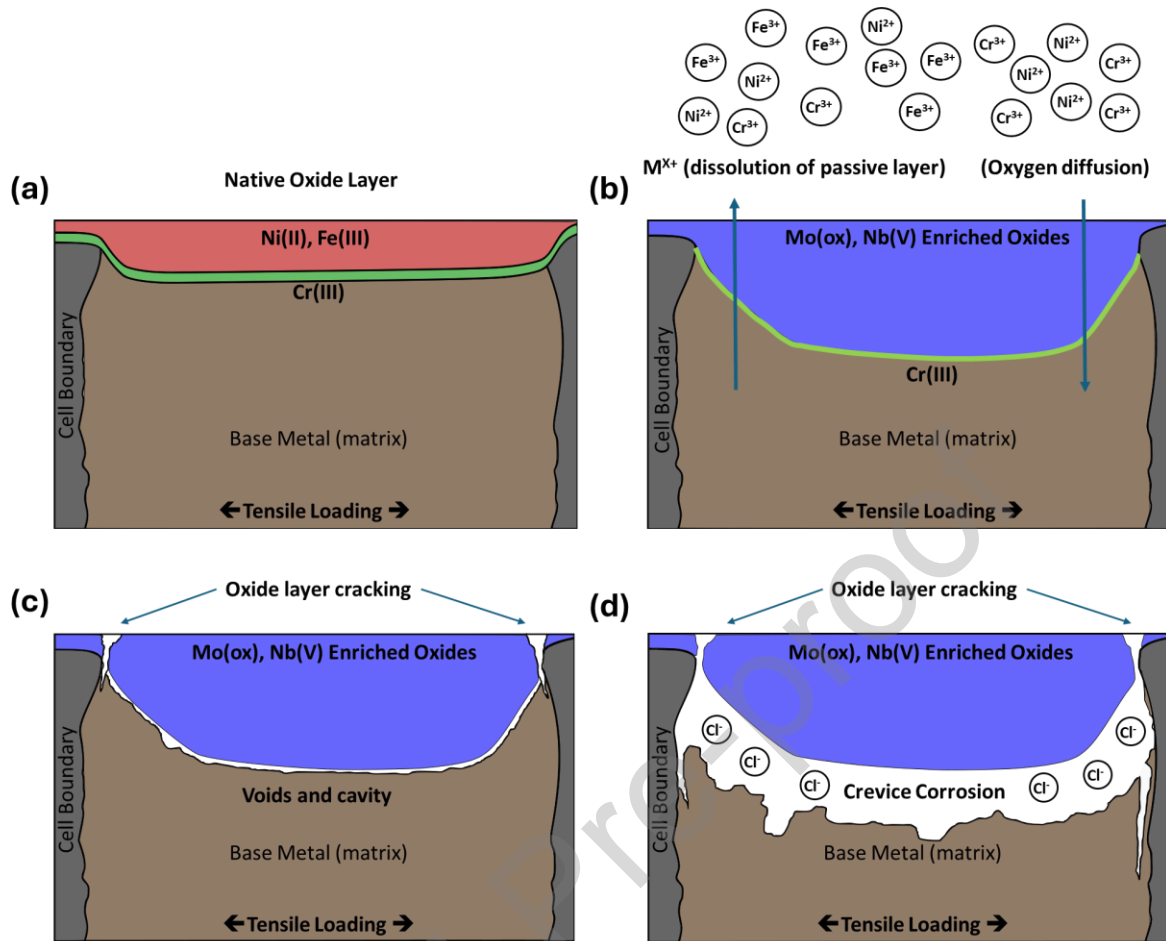
Figure 14. Schematic illustration of passive layer breakdown under tensile loading state, (a) native oxide layer, (b) dissolution of passive layer under tensile loading polarization condition, (c) formation of cracks adjacent to cell boundaries and voids in the interface of oxide layer-base metal, and (d) crevice corrosion beneath the surface oxide layer.

This investigation represents the first steps to establish the link between high-resolution analytical techniques, electrochemical polarization behaviour, and the occurrence of passive layer breakdown in the unique microstructure of additively manufactured Ni-Fe-Cr-based alloys. The mechanism responsible for passive layer breakdown has been proposed based on experimental data obtained through a combination of analytical methods and microcapillary electrochemical techniques. However, further research is required to better understand the interplay between environmental and microstructural factors affecting the kinetics of passive layer degradation. Additionally, it is necessary to investigate the evolution of the passive layer under various environmental conditions to determine the thresholds for passive layer rupture. Moreover, exploring the effects of different loading conditions, beyond the tensile loading employed in this study, is of critical importance and warrants further investigation.

Conclusion

The current investigation aimed to elucidate the true nature of formation and degradation of the passive layer on L-PBF processed Ni-Fe-Cr-based alloy 718 by high-resolution submicron analysis. The study provides significant insights into the breakdown of the passive layer under tensile loading and polarization conditions, considering various factors such as the microstructural characteristics of the alloy, dislocation distribution and behaviour, alloying element interactions at the passive layer interface, and the impact of mechanical stresses on oxide layer stability. The key findings are summarized as:

- SKPFM indicates lower CPD values at cell boundaries compared to interiors in L-PBF processed Ni-Fe-Cr-based alloy 718. Contrary to classical interpretations, cell interiors are more prone to corrosion in chloride environments because of the presence of higher dislocation density in the vicinity of cell's borders.
- Under tensile strain, charge carrier density in the passive layer increases, indicating a more defective passive layer, which consequently leads to more severe corrosion.
- Metallic not oxidized cell boundaries could be detected in the oxide layer formed after electrochemical polarization experiments, which suggests a higher corrosion resistance of cell boundaries.
- External loading in combination with a corrosive environment leads to the rupture and detachment of the passive oxide layer (with crack tips reaching the metal substrate), which creates voids between this ruptured passive oxide layer and the metallic substrate.

The mechanism of corrosion- and stress-induced passive layer breakdown can be summarized as follows: Under external tensile strain and in the presence of a corrosive environment, passive layer breakdown occurs near cells borders (with crack tips occasionally reaching the metallic substrate). This is followed by detachment of the oxide from the metal substrate due to the external loading, creating voids between the oxide and the metal. Penetration of aggressive corrosive media progresses into these voids, further attacking the metal underneath, aggravated by the formation of occluded corrosion cell conditions.

Acknowledgements

Data availability

The raw data required to reproduce these findings can be made available upon reasonable request.

References

[1] D. Herzog, V. Seyda, E. Wycisk, C. Emmelmann, Additive manufacturing of metals, Acta Mater. 117 (2016) 371–392. https://doi.org/10.1016/j.actamat.2016.07.019.

[2] A. Bandyopadhyay, S. Bose, Additive manufacturing, CRC press, 2019.

[3] M.M. Attallah, R. Jennings, X. Wang, L.N. Carter, Additive manufacturing of Ni-based superalloys: The outstanding issues, MRS Bull. 41 (2016) 758–764.

[4] M. Shahwaz, P. Nath, I. Sen, A critical review on the microstructure and mechanical properties correlation of additively manufactured nickel-based superalloys, J. Alloys Compd. 907 (2022) 164530.

[5] Q. Jia, D. Gu, Selective laser melting additive manufacturing of Inconel 718 superalloy parts: Densification, microstructure and properties, J. Alloys Compd. 585 (2014) 713–721.

[6] S. Luo, W. Huang, H. Yang, J. Yang, Z. Wang, X. Zeng, Microstructural evolution and corrosion behaviors of Inconel 718 alloy produced by selective laser melting following different heat treatments, Addit. Manuf. 30 (2019) 100875. https://doi.org/10.1016/j.addma.2019.100875.

[7] W.M. Tucho, V. Hansen, Characterization of SLM-fabricated Inconel 718 after solid solution and precipitation hardening heat treatments, J. Mater. Sci. 54 (2019) 823–839. https://doi.org/10.1007/s10853-018-2851-x.

[8] W.M. Tucho, P. Cuvillier, A. Sjolyst-Kverneland, V. Hansen, Microstructure and hardness studies of Inconel 718 manufactured by selective laser melting before and after solution heat treatment, Mater. Sci. Eng. A 689 (2017) 220–232. https://doi.org/10.1016/j.msea.2017.02.062.

[9] W.M. Tucho, V. Hansen, Studies of Post-Fabrication Heat Treatment of L-PBF-Inconel 718: Effects of Hold Time on Microstructure, Annealing Twins, and Hardness, Metals 11 (2021) 266. https://doi.org/10.3390/met11020266.

[10] A. Stachowiak, D. Wieczorek, K. Gruber, D. Bartkowski, A. Bartkowska, D. Ulbrich, Comparison of tribocorrosion resistance of Inconel® 718 alloy manufactured by conventional method and laser powder bed fusion method, Tribol. Int. 182 (2023) 108368. https://doi.org/10.1016/j.triboint.2023.108368.

[11] P. Murmey, U. Nichul, M. Chikode, V. Hiwarkar, Effect of Post-processing on Corrosion Behavior of LPBF Built Inconel 718 Alloy, JOM 75 (2023) 32–44. https://doi.org/10.1007/s11837-022-05565-w.

[12] H. Shi, T. Wu, Q. Gong, W. Ding, Y. Chai, A. Weisenburger, L. Chang, Z. Zhang, K. Wang, J. Richter, T. Niendorf, G. Müller, Hot corrosion behavior of additively manufactured stainless steel 316L and Inconel 718 in MgCl2/KCl/NaCl chloride salts at 700 °C, Corros. Sci. 207 (2022) 110561. https://doi.org/10.1016/j.corsci.2022.110561.

[13] O.V. Mythreyi, B.K. Nagesha, R. Jayaganthan, Microstructural evolution & corrosion behavior of Laser –powder-bed–fused Inconel 718 subjected to surface and heat treatments, J. Mater. Res. Technol. 19 (2022) 3201–3215. https://doi.org/10.1016/j.jmrt.2022.05.123.

[14] T. Thuneman, K.S. Raja, I. Charit, Room Temperature Corrosion Behavior of Selective Laser Melting (SLM)-Processed Ni-Fe Superalloy (Inconel 718) in 3.5% NaCl Solution at Different pH Conditions: Role of Microstructures, Crystals 14 (2024) 89. https://doi.org/10.3390/cryst14010089.

[15] Y. Qiao, W. Zhang, N. AlMasoud, X. Shen, S. Zheng, T.S. Alomar, Z.M. El-Bahy, M.M. Ibrahim, H. Algadi, W. Liu, Improved passivation and anticorrosion behaviors of selective laser melted Inconel 718 alloy in acidic solutions, Adv. Compos. Hybrid Mater. 6 (2023) 204. https://doi.org/10.1007/s42114-023-00786-2.

[16] Y. Tang, X. Shen, Y. Qiao, L. Yang, J. Chen, D. Lu, Z. Zhang, Corrosion Behavior of a Selective Laser Melted Inconel 718 Alloy in a 3.5 wt.% NaCl Solution, J. Mater. Eng. Perform. 30 (2021) 5506–5514. https://doi.org/10.1007/s11665-021-05909-8.

[17] A. Yazdanpanah, R.I. Revilla, M. Franceschi, A. Fabrizi, S. Khademzadeh, M. Khodabakhshi, I. De Graeve, M. Dabalà, Unveiling the impact of laser power variations on microstructure, corrosion, and stress-assisted surface crack initiation in laser powder bed fusion-processed Ni-Fe-Cr alloy 718, Electrochimica Acta 476 (2024) 143723. https://doi.org/10.1016/j.electacta.2023.143723.

[18] H. Dai, S. Zhang, Y. Li, J. Yu, Y. Kuang, F. Xuan, X. Chen, Stress corrosion cracking behavior of 316 L manufactured by different additive manufacturing techniques in hydrofluoric acid vapor, J. Mater. Sci. Technol. 191 (2024) 33–48. https://doi.org/10.1016/j.jmst.2023.12.041.

[19] R. Santamaria, K. Wang, M. Salasi, M. Salem, P. Lours, M. Iannuzzi, M.Z. Quadir, Stress Corrosion Cracking Behavior of Austenitic Stainless Steel 316L Produced Using Laser-Based Powder Bed Fusion, Corrosion 79 (2023) 944–956. https://doi.org/10.5006/4311.

[20] Z. Que, T. Riipinen, S. Goel, A. Revuelta, T. Saario, K. Sipilä, A. Toivonen, SCC behaviour of laser powder bed fused 316L stainless steel in high-temperature water at 288 °C, Corros. Sci. 214 (2023) 111022. https://doi.org/10.1016/j.corsci.2023.111022.

[21] M. Cabrini, S. Lorenzi, C. Testa, F. Carugo, T. Pastore, D. Manfredi, S. Biamino, G. Marchese, S. Parizia, F. Scenini, Stress Corrosion Cracking of Additively Manufactured Alloy 625, Materials 14 (2021) 6115. https://doi.org/10.3390/ma14206115.

[22] A. Yazdanpanah, M. Franceschi, P. Rebesan, M. Dabalà, Correlation of Lack of Fusion Pores with Stress Corrosion Cracking Susceptibility of L-PBF 316L: Effect of Surface Residual Stresses, Materials 15 (2022) 7151. https://doi.org/10.3390/ma15207151.

[23] C. Gasparrini, J.O. Douglas, A. Yazdanpanah, R. Stroud, G. Divitini, M. Dabalà, G.G. Scatigno, S. Pedrazzini, M.R. Wenman, D. Badocco, P. Pastore, N. Terranova, G. Mariano, F. Dacquait, M.D. Palma, R. Villari, P. Sonato, Corrosion of 316L exposed to highly concentrated borated water used as shield in nuclear fusion experimental reactors cooling circuits, Corros. Sci. 230 (2024) 111902. https://doi.org/10.1016/j.corsci.2024.111902.

[24] A. Yazdanpanah, L. Pezzato, M. Dabalà, Stress corrosion cracking of AISI 304 under chromium variation within the standard limits: Failure analysis implementing microcapillary method, Eng. Fail. Anal. 142 (2022) 106797. https://doi.org/10.1016/j.engfailanal.2022.106797.

[25] A. Yazdanpanah, M. Franceschi, R.I. Revilla, S. Khademzadeh, I. De Graeve, M. Dabalà, Revealing the stress corrosion cracking initiation mechanism of alloy 718 prepared by laser powder bed fusion assessed by microcapillary method, Corros. Sci. 208 (2022) 110642. https://doi.org/10.1016/j.corsci.2022.110642.

[26] R.I. Revilla, Methods—On the Application of Ambient Scanning Kelvin Probe Force Microscopy to Understand Micro-Galvanic Corrosion Phenomena: Interpretation and Challenges, J. Electrochem. Soc. (2023).

[27] A. Yazdanpanah, N. Capuzzo, M. Khodabakhshi, M. Dabalà, Evaluation of stress-assisted corrosion performance of L-PBF processed Ti6Al4V: A microcapillary electrochemical approach, Eng. Fail. Anal. 166 (2024) 108891. https://doi.org/10.1016/j.engfailanal.2024.108891.

[28] J. Li, Z. Zhao, P. Bai, H. Qu, B. Liu, L. Li, L. Wu, R. Guan, H. Liu, Z. Guo, Microstructural evolution and mechanical properties of IN718 alloy fabricated by selective laser melting following different heat treatments, J. Alloys Compd. 772 (2019) 861–870. https://doi.org/10.1016/j.jallcom.2018.09.200.

[29] K. Moussaoui, W. Rubio, M. Mousseigne, T. Sultan, F. Rezai, Effects of Selective Laser Melting additive manufacturing parameters of Inconel 718 on porosity, microstructure and mechanical properties, Mater. Sci. Eng. A 735 (2018) 182–190.

[30] C. Kumara, A.R. Balachandramurthi, S. Goel, F. Hanning, J. Moverare, Toward a better understanding of phase transformations in additive manufacturing of Alloy 718, Materialia 13 (2020) 100862.

[31] J. Zheng, S. Chen, L. Jiang, X.-X. Ye, C. Xu, Z. Li, Effect of carbon content on the microstructure and mechanical properties of NiCrFe-7A alloys synthesized by wire arc additive manufacturing, Mater. Sci. Eng. A 842 (2022) 142925. https://doi.org/10.1016/j.msea.2022.142925.

[32] E.A. Trillo, L.E. Murr, Effects of carbon content, deformation, and interfacial energetics on carbide precipitation and corrosion sensitization in 304 stainless steel, Acta Mater. 47 (1998) 235–245. https://doi.org/10.1016/S1359-6454(98)00322-X.

[33] M. Wang, M. Song, G.S. Was, J.L. Nelson, The roles of thermal mechanical treatment and δ phase in the stress corrosion cracking of alloy 718 in primary water, Corros. Sci. 160 (2019) 108168. https://doi.org/10.1016/j.corsci.2019.108168.

[34] R.I. Revilla, Methods—On the Application of Ambient Scanning Kelvin Probe Force Microscopy to Understand Micro-Galvanic Corrosion Phenomena: Interpretation and Challenges, J. Electrochem. Soc. 170 (2023) 011501. https://doi.org/10.1149/1945-7111/acafab.

[35] M. Da Cunha Belo, N.E. Hakiki, M.G.S. Ferreira, Semiconducting properties of passive films formed on nickel–base alloys type Alloy 600: influence of the alloying elements, Electrochimica Acta 44 (1999) 2473–2481. https://doi.org/10.1016/S0013-4686(98)00372-7.

[36] S. Choudhary, V. Cruz, A. Pandey, S. Thomas, N. Birbilis, Element-resolved electrochemical analysis of the passivity of additively manufactured stainless steel 316L, Corros. Sci. 189 (2021) 109576. https://doi.org/10.1016/j.corsci.2021.109576.

[37] D.D. Macdonald, PassivityÐthe key to our metals-based civilization, Pure Appl Chem 71 (1999) 951–978.

[38] E. Sikora, D.D. Macdonald, Nature of the passive film on nickel, Electrochimica Acta 48 (2002) 69–77. https://doi.org/10.1016/S0013-4686(02)00552-2.

[39] B. Lovreček, J. Sefaja, Semiconducting aspects of the passive layer on chromium, Electrochimica Acta 17 (1972) 1151–1155. https://doi.org/10.1016/0013-4686(72)90031-X.

[40] N.B. Hakiki, S. Boudin, B. Rondot, M. Da Cunha Belo, The electronic structure of passive films formed on stainless steels, Corros. Sci. 37 (1995) 1809–1822. https://doi.org/10.1016/0010-938X(95)00084-W.

[41] N.E. Hakiki, Comparative study of structural and semiconducting properties of passive films and thermally grown oxides on AISI 304 stainless steel, Corros. Sci. 53 (2011) 2688–2699. https://doi.org/10.1016/j.corsci.2011.05.012.

[42] A. Machet, A. Galtayries, S. Zanna, L. Klein, V. Maurice, P. Jolivet, M. Foucault, P. Combrade, P. Scott, P. Marcus, XPS and STM study of the growth and structure of passive films in high temperature water on a nickel-base alloy, Electrochimica Acta 49 (2004) 3957–3964. https://doi.org/10.1016/j.electacta.2004.04.032.

[43] N.E. Hakiki, M.D.C. Belo, A.M.P. Simões, M.G.S. Ferreira, Semiconducting Properties of Passive Films Formed on Stainless Steels: Influence of the Alloying Elements, J. Electrochem. Soc. 145 (1998) 3821. https://doi.org/10.1149/1.1838880.

[44] M.F. Montemor, M.G.S. Ferreira, N.E. Hakiki, M. Da Cunha Belo, Chemical composition and electronic structure of the oxide films formed on 316L stainless steel and nickel based alloys in high temperature aqueous environments, Corros. Sci. 42 (2000) 1635–1650. https://doi.org/10.1016/S0010-938X(00)00012-3.

[45] A. Yazdanpanah, G. Pagot, M. Franceschi, P. Rebesan, M. Venturin, J. Botinha, B. Gerhmann, I. De Graeve, V.D. Noto, R.I. Revilla, M. Dabalà, Mechanism of alteration in passivity of additively manufactured Ni-Fe-Cr Alloy 718 caused by minor carbon variation, Electrochimica Acta 503 (2024) 144925. https://doi.org/10.1016/j.electacta.2024.144925.

[46] M. da Cunha Belo, M. Walls, N.E. Hakiki, J. Corset, E. Picquenard, G. Sagon, D. Noël, Composition, structure and properties of the oxide films formed on the stainless steel 316L in a primary type PWR environment, Corros. Sci. 40 (1998) 447–463. https://doi.org/10.1016/S0010-938X(97)00158-3.

[47] N.E. Hakiki, M.F. Montemor, M.G.S. Ferreira, M. da Cunha Belo, Semiconducting properties of thermally grown oxide films on AISI 304 stainless steel, Corros. Sci. 42 (2000) 687–702. https://doi.org/10.1016/S0010-938X(99)00082-7.

[48] M.G.S. Ferreira, N.E. Hakiki, G. Goodlet, S. Faty, A.M.P. Simões, M. Da Cunha Belo, Influence of the temperature of film formation on the electronic structure of oxide films formed on 304 stainless steel, Electrochimica Acta 46 (2001) 3767–3776. https://doi.org/10.1016/S0013-4686(01)00658-2.

[49] R.D. Gryse, W.P. Gomes, F. Cardon, J. Vennik, On the Interpretation of Mott-Schottky Plots Determined at Semiconductor/Electrolyte Systems, J. Electrochem. Soc. 122 (1975) 711. https://doi.org/10.1149/1.2134298.

[50] A. Fattah-alhosseini, F. Soltani, F. Shirsalimi, B. Ezadi, N. Attarzadeh, The semiconducting properties of passive films formed on AISI 316 L and AISI 321 stainless steels: A test of the point defect model (PDM), Corros. Sci. 53 (2011) 3186–3192. https://doi.org/10.1016/j.corsci.2011.05.063.

[51] D.D. Macdonald, The history of the Point Defect Model for the passive state: A brief review of film growth aspects, Electrochimica Acta 56 (2011) 1761–1772.

[52] M. da Cunha Belo, M. Walls, N.E. Hakiki, J. Corset, E. Picquenard, G. Sagon, D. Noël, Composition, structure and properties of the oxide films formed on the stainless steel 316L in a primary type PWR environment, Corros. Sci. 40 (1998) 447–463. https://doi.org/10.1016/S0010-938X(97)00158-3.

[53] C. Örnek, C. Leygraf, J. Pan, On the Volta potential measured by SKPFM – fundamental and practical aspects with relevance to corrosion science, Corros. Eng. Sci. Technol. 54 (2019) 185–198. https://doi.org/10.1080/1478422X.2019.1583436.

[54] K. Yasakau, Application of AFM-Based Techniques in Studies of Corrosion and Corrosion Inhibition of Metallic Alloys, Corros. Mater. Degrad. 1 (2020) 345–372. https://doi.org/10.3390/cmd1030017.

[55] G.M. Volpato, U. Tetzlaff, M.C. Fredel, A comprehensive literature review on laser powder bed fusion of Inconel superalloys, Addit. Manuf. 55 (2022) 102871. https://doi.org/10.1016/j.addma.2022.102871.

[56] M.P. Haines, V.V. Rielli, S. Primig, N. Haghdadi, Powder bed fusion additive manufacturing of Ni-based superalloys: a review of the main microstructural constituents and characterization techniques, J. Mater. Sci. 57 (2022) 14135–14187. https://doi.org/10.1007/s10853-022-07501-4.

[57] V.B. Vukkum, R.K. Gupta, Review on corrosion performance of laser powder-bed fusion printed 316L stainless steel: Effect of processing parameters, manufacturing defects, post-processing, feedstock, and microstructure, Mater. Des. 221 (2022) 110874. https://doi.org/10.1016/j.matdes.2022.110874.

[58] M. Iannuzzi, K.L. Vasanth, G.S. Frankel, Unusual Correlation between SKPFM and Corrosion of Nickel Aluminum Bronzes, J. Electrochem. Soc. 164 (2017) C488. https://doi.org/10.1149/2.0391709jes.

[59] S. Lozano-Perez, D.W. Saxey, T. Yamada, T. Terachi, Atom-probe tomography characterization of the oxidation of stainless steel, Scr. Mater. 62 (2010) 855–858. https://doi.org/10.1016/j.scriptamat.2010.02.021.

[60] C.M. Hussain, C. Verma, J. Aslam, R. Aslam, S. Zehra, 4 - Crevice corrosion, in: C.M. Hussain, C. Verma, J. Aslam, R. Aslam, S. Zehra (Eds.), Handb. Corros. Eng., Elsevier, 2023: pp. 55–69. https://doi.org/10.1016/B978-0-323-95185-2.00004-6.

CRediT authorship contribution statement

Arshad Yazdanpanah: Conceptualization, Writing – review & editing, Writing – original draft, Visualization, Validation, Software, Methodology, Investigation, Formal analysis, Data curation. **Reynier I. Revilla:** Writing – review & editing, Writing – original draft, Visualization, Validation, Methodology, Investigation, Formal analysis, Data curation. **Mattia Franceschi:** Software, Investigation, Formal analysis. **Gioele Pagot:** Writing – original draft, Software, Investigation, Data curation. **Mona Khodabakhshi:** Software, Investigation, Data curation, Visualization. **Iris De Graeve:** Writing – review & editing, Supervision, Resources. **Vito Di Noto:** Writing – review & editing, Supervision. **Manuele Dabalà:** Writing – review & editing, Supervision, Resources, Project administration, Funding acquisition. **Sergio Lozano-Perez:** Writing – original draft, Writing – review & editing, Supervision, Resources, Investigation, Formal analysis, Data curation, Project administration.

Declaration of Competing Interest

The authors declare that they have no known competing financial interests or personal relationships that could have appeared to influence the work reported in this paper.

Highlights:

- External loading causes oxide layer rupture adjacent to cell boundaries
- Metallic cell boundaries within the oxide layer suggest higher corrosion resistance
- Voids form between the metal and oxide layer promoting aggressive ion penetration
- Crevice corrosion occurs as a result of void coalescence beneath the oxide layer